Acoustic Black Holes in a Spinning Beam

Yuhang Wang
College of Power and Energy Engineering,
Harbin Engineering University,
Harbin 150001, China
e-mail: wangyuhangheu@163.com

Li Cheng
Department of Mechanical Engineering,
The Hong Kong Polytechnic University,
Hong Kong 999077, China
e-mail: li.cheng@polyu.edu.hk

Jingtao Du[1]
College of Power and Energy Engineering,
Harbin Engineering University,
Harbin 150001, China
e-mail: dujingtao@hrbeu.edu.cn

Yang Liu
College of Power and Energy Engineering,
Harbin Engineering University,
Harbin 150001, China
e-mail: liuyangly91@hrbeu.edu.cn

Through creating slow waves in structures, acoustic black hole (ABH) shows promise for potential vibration control applications. However, it remains unclear whether such phenomena can still occur in a structure undergoing high-speed spinning, and if so, what is the interplay among various system parameters and what are the underpinning physical mechanisms. To address this issue, this work establishes a semi-analytical model for a spinning ABH beam based on Euler–Bernoulli beam theory under the energy framework. After its validation, the model is used to reveal a few important vibration features pertinent to the spinning ABH beam through examining its dynamics, modal properties, and energy flow. It is shown that the spinning-induced centrifugal effects generate hardening effects inside the structure, thus increasing the overall structural stiffness and stretching the wavelength of the modal deformation of flexural waves as compared with its counterpart at rest. Meanwhile, energy flow to the ABH portion of the beam is also adversely affected. As a result, the ABH-induced overall damping enhancement effect of the viscoelastic coating, as observed in conventional ABH beam at rest, is impaired. Nevertheless, the study confirms that typical ABH features, in terms of wave compression, energy trapping, and dissipation, though affected by the spinning effects, are still persistent in a high-speed spinning structure. This provides the theoretical basis for the ABH phenomena in the design of high-performance rotating mechanical components such as turbine blades.
[DOI: 10.1115/1.4056791]

Keywords: acoustic black hole, spinning beam, power flow, wave compression, energy dissipation

1 Introduction

As a novel passive control means, the acoustic black hole (ABH) allows for the design of lightweight and highly damped structures, conducive for numerous vibration and noise control applications. Through a continuous decrease of structural thickness according to a power-law relationship, the group velocity of the incident flexural waves gradually decreases to zero, thus minimizing wave reflections and generating high-density energy concentration at the tip of an ideal ABH wedge [1]. The deployment of an energy-absorbing layer such as viscoelastic coating over the tapered ABH region allows compensating for the adverse effects caused by the unavoidable residual thickness at the wedge tip, referred to as thickness truncation [2,3]. The last decade has witnessed an increasing research effort devoted to various aspects pertinent to ABH phenomena as well as their applications. Typical examples include the modeling, numerical analyses, and experimental assessment of the ABH effects in both beams [4,5] and plate structures [6–8] as well as their applications in structural design [9,10], phononic crystals [11,12], energy harvesting [13,14], and sound radiation control [15,16]. A comprehensive review on the topic can be found in the open literature [17–19].

Most of the existing ABH studies address structures at rest. Investigations establish that the ABH effect is effective within a wide frequency range above the cut-on frequency. In contrast, no concerted attention was paid to rotating ABH structures in the existing literature, although the idea of using the ABH principle in the design of a spinning turbine blade was conceptually mentioned [20,21]. In fact, rotating structures are commonly encountered in engineering problems, such as gas turbines and turbofans in which blades undergo high-speed spinning. Whether ABH effects still exist, and if so, how they will play out, is a fundamental and open question to be answered. This brings up the need of developing a suitable model to take the spinning effects into account and understanding the influence of spinning effects in the proper ABH context. Intuitively, in contrast with its static counterpart, the spinning-induced centrifugal force would affect the overall structural stiffness distribution, whilst a gradual reduction of the structural stiffness is the cornerstone of the ABH phenomena. Therefore, addressing the aforementioned problems would constitute an interesting scientific topic.

Motivated by this, a semi-analytical model for the dynamic analysis and power flow study of a rotating cantilever ABH beam is established based on the Euler–Bernoulli beam theory, in which the spinning-induced stiffening effect is considered. An improved Fourier series expansion is employed to arrive at an approximate solution, which informs on the dynamic responses and structural intensity distribution inside the spinning ABH beams. The accuracy of the semi-analytical model is verified through comparison with the results from finite element method (FEM). Based on the established model, influences of the rotating effect on ABH beams without and with damping layers are investigated in terms of dynamic response, mean energy distribution, and energy transmission.

2 Theoretical Formulation

2.1 Model Description. Consider the transverse vibration of a rotating ABH beam illustrated in Fig. 1. The beam, with a length L and a constant width b, has a thickness profile $h(x)$ and is symmetrically covered by damping layers of thickness h_d from x_{d1} to x_{d2}, in which $h(x)$ comprises a uniform portion h_b and power-law profiled ABH portion $h_{ABH}(x) = \varepsilon(L_{total}\text{-}x)^m$ with ε being a constant and m a power-law index, which follows the following piecewise function

[1]Corresponding author.

Contributed by the Technical Committee on Vibration and Sound of ASME for publication in the Journal of Vibration and Acoustics. Manuscript received January 17, 2022; final manuscript received January 21, 2023; published online February 28, 2023. Assoc. Editor: Fabio Semperlotti.

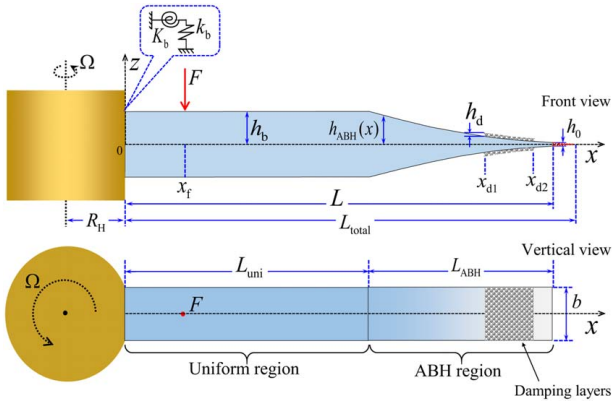

Fig. 1 Schematic diagram of a rotating cantilever ABH beam

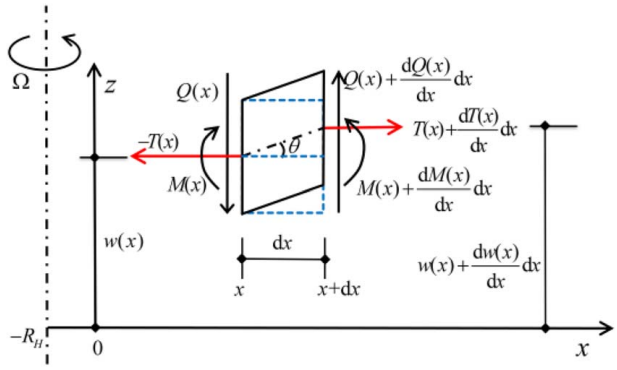

Fig. 2 Internal and external forces and moments applied on an incremental length *dx* of rotating ABH beam

$$h(x)=\begin{cases} h_b, & 0\le x<L_{uni} \\ h_{ABH}(x), & L_{uni}\le x\le L \end{cases} \tag{1}$$

Using the coordinate system shown in Fig. 1 and letting L_{total} be the total length of ABH beam without any truncation and h_0 the truncation thickness at its free tip, one has

$$\begin{cases} L_{total}=(h_b/\varepsilon)^{1/m}+L_{uni} \\ h_0=2\varepsilon(L_{total}-L)^m \end{cases} \tag{2}$$

Assume the ABH beam rotates at a constant angular velocity Ω with a hub radius R_H as shown in Fig. 1. The right hand-side end of the non-uniform portion of the beam is set as free, and the other end is elastically constrained by a set of artificial translational and rotational springs, with stiffness k_b and K_b, respectively. Hence, a cantilever boundary can be simulated by setting a large enough k_b and K_b, as compared with the stiffness of the beam itself [9]. Inherent material damping in the beam and that of the damping layers are included using complex Young's modulus $E=E(1+j\eta)$, with $j=\sqrt{-1}$ and ξ being the damping loss factor, for which different values are taken for the beam and damping layers, respectively.

To analyze the force equilibrium relationship in the ABH beam under rotational motion, an infinitesimal element is used. As shown in Fig. 2, the axial load $T(x)$ due to centrifugal force along the x-direction is applied on the both sides of the element, and the relationship between centrifugal force and rotating speed Ω can be expressed as

$$-\frac{dT(x)}{dx}+\rho b\Omega^2 h(x)(R_H+x)=0 \tag{3}$$

where Ω is the rotating speed in rad/s. Then, $T(x)$ can be obtained by integrating Eq. (3) from x to L, namely

$$T(x)=\rho b\Omega^2\int_x^L h(x)(R_H+x)dx \tag{4}$$

Assuming that damping layers are thin and light enough, the centrifugal force introduced by the damping layers is deemed negligible. Considering the thickness profile $h(x)$ of ABH beam, the centrifugal force inside the beam $T(x)$ writes

$$T(x)=\begin{cases} 2\rho bh_b\Omega^2\int_x^{L_{uni}}(R_H+x)dx+2\rho b\Omega^2\int_{L_{uni}}^{L}h_{ABH}(x)(R_H+x)dx, & 0\le x<L_{uni} \\ 2\rho b\Omega^2\int_x^{L}h_{ABH}(x)(R_H+x)dx, & L_{uni}\le x\le L \end{cases} \tag{5}$$

Based on Euler–Bernoulli beam theory, the bending moment of ABH beam is

$$M(x)=\mathrm{EI}(x)\frac{d^2w(x)}{dx^2} \tag{6}$$

in which $I(x)=bh^3(x)/12$ is the second moment of area of the beam cross section and $w(x)$ the transverse displacement of the flexural vibration of the beam. The moment equilibrium equation at the point $(x+\mathrm{d}x)$ writes

$$Q(x)dx+dM(x)-T(x)dw(x)=0 \tag{7}$$

Then, the shear force $Q(x)$ under the rotating condition can be derived as

$$Q(x)=T(x)\frac{dw(x)}{dx}-\frac{dM(x)}{dx} \tag{8}$$

2.2 Energy Formulation for the Rotating Acoustic Black Hole Beam. Adopting Euler–Bernoulli beam theory and with rotational stiffening effect, both the bending and stretching deformations of the beam are considered. The transverse displacement and axial deformation field of the beam write

$$w(x,\,t)=\bar{w}(x)e^{j\omega t} \tag{9}$$

$$u(x,\,t)=u_T(x)-z\frac{\partial w(x,\,t)}{\partial x} \tag{10}$$

where $w(x,\,t)$ is the flexural displacement of the beam along the z-direction of the neutral axis of the beam with $\bar{w}(x)$ denoting the spatial displacement field. For a constant rotating speed Ω, $u_T(x)$ is the axial displacement due to the centrifugal force $T(x)$ alone, which is uniform over the cross section of the beam. This yields

$$\frac{\partial u_T(x)}{\partial x}=\varepsilon_T(x)=\frac{T(x)}{EA(x)} \tag{11}$$

in which $\varepsilon_T(x)$ is the strain due to the centrifugal force $T(x)$. According to the coordinate system shown in Fig. 2, considering the axial and flexural displacements of the beam, the deformation of the element $\mathrm{d}x$ can be expressed by the axial and flexure directional

components [22]. On the left-hand facet of the element, at a distance $\bar{z}$ from the neutral axis, $\{x_1, z_1\}$ writes

$$\{x_1, z_1\} = \{(x + u_T(x) - \bar{z}\frac{\partial w(x,t)}{\partial x}), (\bar{z} + w(x,t))\} \tag{12}$$

The corresponding point on the right-hand facet follows:

$$\{x_2, z_2\} = \begin{Bmatrix} (x + u_T(x) - \bar{z}\frac{\partial w(x,t)}{\partial x} + \left(1 + \frac{du_T(x)}{dx} - \bar{z}\frac{\partial^2 w(x,t)}{\partial x^2}\right)dx), \\ \left(\bar{z} + w(x,t) + \frac{\partial w(x,t)}{\partial x}dx\right) \end{Bmatrix} \tag{13}$$

So, the strain of the element at a distance $\bar{z}$ from the neutral axis can be expressed as

$$\begin{aligned} \varepsilon(x,z) &= \frac{\Delta L}{dx} = \frac{\{(z_2 - z_1)^2 + (x_2 - x_1)^2\}^{1/2} - dx}{dx} \\ &= \left\{\left(1 + \frac{du_T(x)}{dx} - \bar{z}\frac{\partial^2 w(x,t)}{\partial x^2}\right)^2 + \left(\frac{\partial w(x,t)}{\partial x}\right)^2\right\}^{1/2} - 1 \\ &\cong \left\{1 + 2\left(\frac{du_T(x)}{dx} - \bar{z}\frac{\partial^2 w(x,t)}{\partial x^2}\right) + \left(\frac{\partial w(x,t)}{\partial x}\right)^2\right\}^{1/2} - 1 \quad \cdots(a) \\ &\cong \frac{1}{2}\left\{2\left(\frac{du_T(x)}{dx} - \bar{z}\frac{\partial^2 w(x,t)}{\partial x^2}\right) + \left(\frac{\partial w(x,t)}{\partial x}\right)^2\right\} \quad \cdots(b) \\ &= \frac{du_T(x)}{dx} - \bar{z}\frac{\partial^2 w(x,t)}{\partial x^2} + \frac{1}{2}\left(\frac{\partial w(x,t)}{\partial x}\right)^2 \end{aligned} \tag{14}$$

where ΔL is the incremental length in the x-axis direction of the element. Based on the Euler–Bernoulli beam theory and small vibration assumption, Steps (a) and (b) can be derived approximately via the Equivalent Infinitesimal Substitution Formula $(1 + x_0)^{\alpha} - \alpha x_0 + 1$ and $(1 + x_0)^{\alpha} - 1 - \alpha x_0$, respectively

Then, the potential energy stored in the beam can be derived as

$$\begin{aligned} \mathrm{PE}_{beam} &= \iiint_V \frac{E(\varepsilon(x,z))^2}{2} dV = \frac{E}{2}\int_A \int_0^L \left(\frac{\partial u_T(x)}{\partial x}\right)^2 dx dA \\ &+ \frac{E}{2}\int_A \int_0^L z^2 \left(\frac{\partial^2 w(x,t)}{\partial x^2}\right)^2 dx dA \\ &+ \frac{E}{2}\int_A \int_0^L \left(\frac{\partial w(x,t)}{\partial x}\right)^2 \left(\frac{\partial u_T(x)}{\partial x}\right) dx dA \\ &+ \frac{E}{2}\int_A \int_0^L \frac{1}{4}\left(\frac{\partial w(x,t)}{\partial x}\right)^4 dx dA \end{aligned} \tag{15}$$

The last term of Eq. (15) is a higher-order small one to be neglected here. Since the neutral axis passes through the centroid and the area $A(x)$ and the second moment of area $I(x)$ of the cross section are, respectively, given by $A(x) = \int_A dA$ and $I(x) = \int_A z^2 dA$, the potential energy PE can be simplified as

$$\mathrm{PE}_{beam} = \frac{1}{2}\begin{bmatrix} \int_0^L \mathrm{EA}(x)\left(\frac{\partial u_T(x)}{\partial x}\right)^2 dx + \int_0^L \mathrm{EI}(x)\left(\frac{\partial^2 w(x,t)}{\partial x^2}\right)^2 dx \\ + \int_0^L \mathrm{EA}(x)\frac{\partial u_T(x)}{\partial x}\left(\frac{\partial w(x,t)}{\partial x}\right)^2 dx \end{bmatrix} \tag{16}$$

Substituting Eq. (11) into Eq. (16) to express $[\partial u_T(x)/\partial x]$ in terms of force $T(x)$ and supplement the potential energy associated with boundary restraining springs, the potential energy for such rotating ABH beam can be further written as

$$\mathrm{PE}_{beam} = \frac{1}{2}\begin{bmatrix} C_1 + \int_0^L \mathrm{EI}(x)\left(\frac{\partial^2 w(x,t)}{\partial x^2}\right)^2 dx + \int_0^L T(x)\left(\frac{\partial w(x,t)}{\partial x}\right)^2 dx \\ + K_b\left(\frac{\partial w(x,t)}{\partial x}\right)^2_{x=0} + k_b(w(x,t))^2_{x=0} \end{bmatrix} \tag{17}$$

in which,

$$C_1 = \int_0^L \mathrm{EA}(x)\left(\frac{\partial u_T(x)}{\partial x}\right)^2 dx \tag{18}$$

In the energy expression, the axial deformation due to rotating motion introduces a term C_1 in the total potential energy expression, which after integration over x becomes a constant. Then, the total potential energy expression, which takes the damping layers into account, writes

$$\mathrm{PE} = \frac{1}{2}\begin{bmatrix} C_1 + E_b\int_0^L I(x)\left(\frac{\partial^2 w(x,t)}{\partial x^2}\right)^2 dx + E_d\int_{x_{d1}}^{x_{d2}} I_d(x)\left(\frac{\partial^2 w(x,t)}{\partial x^2}\right)^2 dx \\ + \int_0^L T(x)\left(\frac{\partial w(x,t)}{\partial x}\right)^2 dx + K_b\left(\frac{\partial w(x,t)}{\partial x}\right)^2_{x=0} + k_b(w(x,t))^2_{x=0} \end{bmatrix} \tag{19}$$

where, $I_d(x) = 2\{3[h_{ABH}(x)]^2 h_d + 3h_{ABH}(x)[h_d]^2 + [h_d]^3\}/3$, is the second moment of area of damping layers. The kinetic energy of rotating ABH beam can be derived from the vibration velocity components of a field point at a distance of z from the neutral axis as

$$v_z = \frac{\partial w(x,t)}{\partial t} \tag{20}$$

With the damping layers, the total kinetic energy KE of the rotating ABH beam writes

$$\mathrm{KE} = \frac{1}{2}\left[\rho_b b\int_0^L 2h(x)\left(\frac{\partial w(x,t)}{\partial t}\right)^2 dx + \rho_d b\int_{x_{d1}}^{x_{d2}} 2h_d\left(\frac{\partial w(x,t)}{\partial t}\right)^2 dx\right] \tag{21}$$

Assuming an external point force applied at $x = x_f$, the work W done can be written as

$$W = \int_0^L F\delta(x - x_f)w(x_f, t)dx \tag{22}$$

where F is the amplitude of external force and $\delta(x)$ is the Dirac delta function to define the applied force position.

2.3 Displacement Function and Solution Procedure. In this work, the boundary condition of the beam is simulated by introducing two types of boundary springs, whose actions are modeled by the potential energy expression PE in the system. Thus, various boundary conditions can be realized by setting the stiffness value of restraining springs accordingly. Therefore, various boundary conditions can be realized by setting the stiffness of restraining springs accordingly. To satisfy the general boundary restraints, Fourier series with supplementary terms is employed to construct the displacement admissible function of the rotating ABH beam as

$$w(x,t) = \left[\sum_{n=0}^{\infty} B_n \cos(\lambda_{Ln}x) + \sum_{i=1}^{4} b_i\zeta_i(x)\right]e^{j\omega t} \tag{23}$$

in which, $\lambda_{Ln} = n\pi/L$, and the four supplementary functions are expressed as

$$\zeta_1(x) = \frac{9L}{4\pi}\sin\left(\frac{\pi x}{2L}\right) - \frac{L}{12\pi}\sin\left(\frac{3\pi x}{2L}\right) \tag{24a}$$

$$\zeta_2(x) = -\frac{9L}{4\pi}\cos\left(\frac{\pi x}{2L}\right) - \frac{L}{12\pi}\cos\left(\frac{3\pi x}{2L}\right) \tag{24b}$$

$$\zeta_3(x) = \frac{L^3}{\pi^3}\sin\left(\frac{\pi x}{2L}\right) - \frac{L^3}{3\pi^3}\sin\left(\frac{3\pi x}{2L}\right) \tag{24c}$$

$$\zeta_4(x) = -\frac{L^3}{\pi^3}\cos\left(\frac{\pi x}{2L}\right) - \frac{L^3}{3\pi^3}\cos\left(\frac{3\pi x}{2L}\right) \tag{24d}$$

In each supplementary function above, the selection of a trigonometric function and their combination are made for the purpose of overcoming the discontinuities in the calculation of the first- and third-order derivatives at the elastic ends. Most importantly, the smoothness achieved allows the calculation of the structural intensity inside the structure, which can hardly be calculated in previous models based on the Rayleigh–Ritz method. More details about the construction of supplementary functions for the structural vibration with general boundary conditions can be referenced in previous papers [5,23].

With the sufficiently smooth admissible function assumed, the system *Lagrangian* writes

$$La = \mathrm{KE} - \mathrm{PE} + W \tag{25}$$

Substituting Eqs. (19), (21), and (22) into Eq. (25) and following standard Rayleigh–Ritz procedure, the system characteristic equation can be derived and written in matrix form as

$$(\mathbf{K} - \omega^2\mathbf{M})\mathbf{R} = \mathbf{\Phi} \tag{26}$$

where $\mathbf{M}$ and $\mathbf{K}$ are the mass and stiffness matrices, respectively; ω is the angular frequency; $\mathbf{R}$ and $\mathbf{\Phi}$ are two vectors containing the coefficients of the improved Fourier series expansion and the external force loading, respectively. $\mathbf{R}$ can be obtained by solving Eq. (26), namely $\mathbf{R} = (\mathbf{K}-\omega^2\mathbf{M})^{-1}\mathbf{\Phi}$. For the free vibration analysis, one can replace the external force vector $\mathbf{\Phi}$ with $\mathbf{0}$. Then, all the modal parameters can be obtained by solving a standard eigenvalue problem. The corresponding physical mode shapes can be plotted by substituting the eigenvectors into the improved Fourier series expansion Eq. (23).

2.4 Structural Intensity. Benefiting from the differential continuity feature of the improved Fourier series displacement expression, all the internal forces required in the subsequent structural intensity analysis can be readily calculated. Since the creation of slow waves leads to energy transport and concentration inside the ABH beam, power flow or structural intensity analysis provides an efficient tool for understanding the energy transport process inside ABH structures, conducive to the exploration of underlying physical mechanisms. In the present case, the structural intensity is defined as a vibrational power flow passing through a given unit cross-sectional area of the ABH beam, namely

$$I_x(x) = \frac{1}{2}\mathrm{Re}\left[Q_x\left(\frac{\partial w(x,t)}{\partial t}\right)^* - M_x\left(\frac{\partial^2 w(x,t)}{\partial x \partial t}\right)^*\right] \tag{27}$$

in which, Q_x and M_x are the shear force and bending moment (shown in Fig. 2), respectively, which can be calculated through the higher-order spatial derivative of the flexure displacement function, namely

$$M_x = \mathrm{EI}(x)\frac{\partial^2 w(x,t)}{\partial x^2} \tag{28}$$

$$Q_x(x) = -\frac{\partial M_x(x,t)}{\partial x} + T(x)\frac{\partial w(x,t)}{\partial x} \tag{29}$$

In this work, the superposition of the standard Fourier series and auxiliary functions guarantee the spatial derivative of various orders to be sufficiently continuous and smooth in the entire solving domain, including the general elastic boundaries. Using $\mathbf{R}$ obtained from Eq. (25), the structural intensity at any field point can be obtained through the post-processing of the vibration displacement response.

3 Results and Discussions

In this section, numerical results will be presented to validate the present model and investigate the dynamic behavior and structural intensity characteristics of a rotating ABH beam. For convenience, some non-dimensional parameters are defined. A non-dimensional resonant frequency λ_n is defined as $\lambda_n = \omega_n/\omega_0$, with $\omega_0 = [EI_0/(\rho b h_b L^4)]$ being the reference frequency using the cross-section parameters of the uniform beam portion, and I_0 is the corresponding moment of inertia. Moreover, a non-dimensional rotating speed is also defined as $\xi = \Omega/\omega_0$ alongside a non-dimensional hub radius as $\gamma = R_H/L$.

3.1 Model Validation. The accuracy of the proposed semi-analytical model is compared with FEM results for validation. Listed in Table 1 are the geometrical and material parameters used in the numerical model. The clamped boundary condition at the root end of the beam (connected to the hub) is realized by assigning large numbers to both stiffness coefficients of the boundary restraining springs: k_b and K_b are assigned as 1×10^{12} (N/m), respectively. Numerical simulations suggest that sufficiently accurate prediction can be achieved by truncating the Fourier series expansion terms to $M = 300$ for the dynamic response and structural intensity analyses of the rotating ABH beam.

FE analysis is implemented in ANSYS using SHELL 63 elements. The non-dimensional rotating speed ratio, ξ, and hub radius ratio, γ, are set at $\xi = 10$ and $\gamma = 1$, respectively. Element size is around 2 mm which is shown to be a sufficient meshing for the current ABH beam to cover the frequency range of interest being discussed in this paper. Further decreasing the mesh size does not generate a noticeable variation in the calculation results. To simulate the rotation-induced stiffening effect, a relative centrifugal load is applied to each FEM node, according to the modeling theory. An error index is defined as $[(\omega_{\mathrm{ANSYS}}\text{-}\omega_{\mathrm{Current}})/\omega_{\mathrm{ANSYS}}]$x100% to assess the agreement between the two sets of results. The comparison in terms of natural frequencies of the first twenty modes is listed in Table 2, which shows that the proposed model offers a reasonably good prediction of the spinning ABH beam dynamics. In addition, the natural frequencies corresponding to torsional modes in the FE model are excluded from this table. The error increases with the mode order at higher frequencies. Nevertheless, the accuracy

Table 1 Geometrical and material parameters of the rotating cantilever ABH beam

Geometrical parameters	
$\varepsilon = 0.125\ \mathrm{m}^{-1}$	$L = 0.32$ m
$m = 2$	$L_{total} = 0.4$ mh
$h_b = 0.005$ m	$h_0 = 0.0016$ m
$L_{uni} = 0.2$ m	$b = 0.01$ m
Material parameters	
Host beam	
$E_b = 71$ GPa	$\rho_b = 2800\ \mathrm{kg/m}^3$
$\eta_b = 0.005$	
Damping layers	
$E_d = 5$ GPa	$\rho_d = 950\ \mathrm{kg/m}^3$
$\eta_d = 0.3$	

Table 2 Comparison of the first twenty natural frequencies of a rotating ABH beam calculated from the current model and FEM with $\xi = 10$ (13,969 rpm) and $\gamma = 1$

Mode no.	Current model (Hz)	ANSYS results (Hz)	Error
1	400.1	400.2	0.0461%
2	951.8	952.6	0.0856%
3	1638.9	1641.1	0.1337%
4	2665.4	2670.3	0.1822%
5	3912.9	3923.0	0.2566%
6	5525.8	5544.1	0.3294%
7	7380.8	7412.5	0.4273%
8	9596.2	9646.6	0.5216%
9	12,073.1	12150.9	0.6403%
10	14895.8	15008.3	0.7494%
11	18000.1	18160.3	0.8820%
12	21431.9	21648.8	1.0018%
13	25165.9	25456.3	1.1407%
14	29207.9	29582.5	1.2663%
15	33572.2	34051.1	1.4065%
16	38225.5	38821.3	1.5346%
17	43219.6	43954.2	1.6713%
18	48486.0	49374.3	1.7992%
19	54108.5	55173.0	1.9294%
20	59989.9	61248.4	2.0547%

achieved is deemed acceptable which can largely cover the frequency range being discussed in the following analyses.

The dynamic response of the beam, in terms of displacement amplitude at the observing point ($x_m = 0.3$ m), under the excitation of a unit point force at $x_f = 0.05$ m, is also calculated and compared with FE results. As shown in Fig. 3, the displacement response is predicted also with an acceptable agreement with the FEM. In fact, these two results agree with each other nicely in the lower frequency range, whilst a distinct resonant peak emerges for the FEM result at 5.9 kHz. Further inspection shows that this extra resonance corresponds to a torsional mode from the FEM simulation, with its corresponding mode shape plotted in the inset of Fig. 3. It can be seen that the uniform end of the ABH beam, clamped at one end and free at the other, incurs a torsional deformation as a result of the adoption of two-dimensional beam elements. This, however, is not considered in the 1D semi-analytical beam model established previously. Except for this particular frequency region, the results from the current model can be regarded as accurate enough and in good agreement with FE results. Therefore, the accuracy and reliability of the established model for vibration analysis of rotating ABH beams are deemed validated.

3.2 Influence of the Rotation Speed on Modal Characteristics of Acoustic Black Hole Beams. Numerical analyses are conducted to study the influence of the spinning on modal characteristics of the ABH beam. The geometric and material parameters used in the simulation model are the same as listed in Table 1. First, nondimensionalized natural frequencies of the rotating ABH beam without a damping layer under different rotating conditions are plotted in Fig. 4 for the first twenty modes.

Four different rotating scenarios are considered. Figure 4 shows the variation of λ_n with respect to the mode order, referenced to the static case denoted by circle symbols. Cases corresponding to three rotating conditions are noted by cross symbols ($\xi = 10$, $\gamma = 0$), the square symbols ($\xi = 10$, $\gamma = 1$), and rhombus symbols ($\xi = 20$, $\gamma = 1$), respectively. A comparison between the static case and the rotating case with $\xi = 10$ and $\gamma = 0$ shows only a slight increase in λ_n, as better shown in the zoomed-in inset of Fig. 4. This trend is obviously amplified when either ξ (non-dimensional rotation speed) or γ (nondimensional hub radius) increases, both leading to the same effects of increasing the structural stiffness and the natural frequencies of the beam due to the centrifugal force-induced hardening effects.

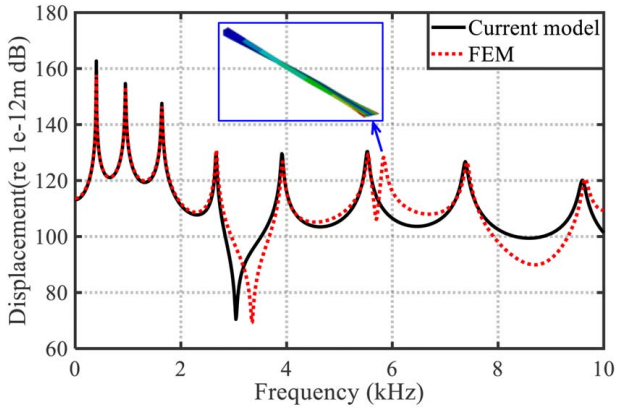

Fig. 3 Comparison of vibration displacement response between the current model and FEM results

A more meaningful investigation is on the corresponding changes in the modal deformation of the beam. Figure 5 shows the first-, fifth-, tenth-, and twentieth-mode shapes of the above spinning ABH beam structure under two selected cases: static case ($\xi = 0$, $\gamma = 0$; solid line) and rotating case ($\xi = 20$, $\gamma = 1$; dot line). From Fig. 5(*a*), an obvious variation can be observed for the first mode, especially over the uniform portion near the clamped end, less obvious when approaching the free end. While the spatial distribution of other modes of the spinning ABH beam basically resembles their static counterparts, a slight stretching of the wavelength, more obvious for modes 5 and 10 (Figs. 5(*b*) and 5(*c*)), is noticed. As discussed before, the spinning-induced centrifugal forces would enhance the structural stiffness, albeit small. Its distribution, however, is non-uniform since its amplitude gradually reduces from the maximum at the clamped end to zero at the free end. As a result, the mode shape under the rotating condition undergoes a noticeable stretching over the uniform portion of the beam, which gradually disappears toward the tip end of the ABH beam. For even higher-order modes, exemplified by twentieth mode depicted in Fig. 5(*d*), the stretching phenomenon disappears. This is understandable since higher-order modes involve high system stiffness even in the static case, so the role played by the incremental stiffness due to the rotation reduces for these modes. As a result, the effect of the rotation on the mode shapes of the ABH beam is not

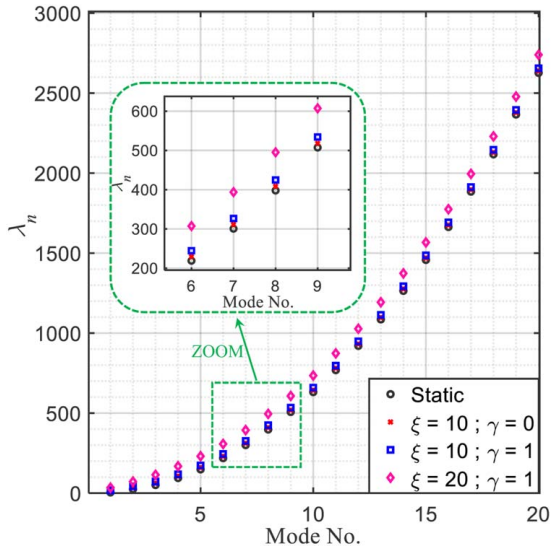

Fig. 4 Comparison of the first 20 modal frequencies of ABH beams under different rotating conditions

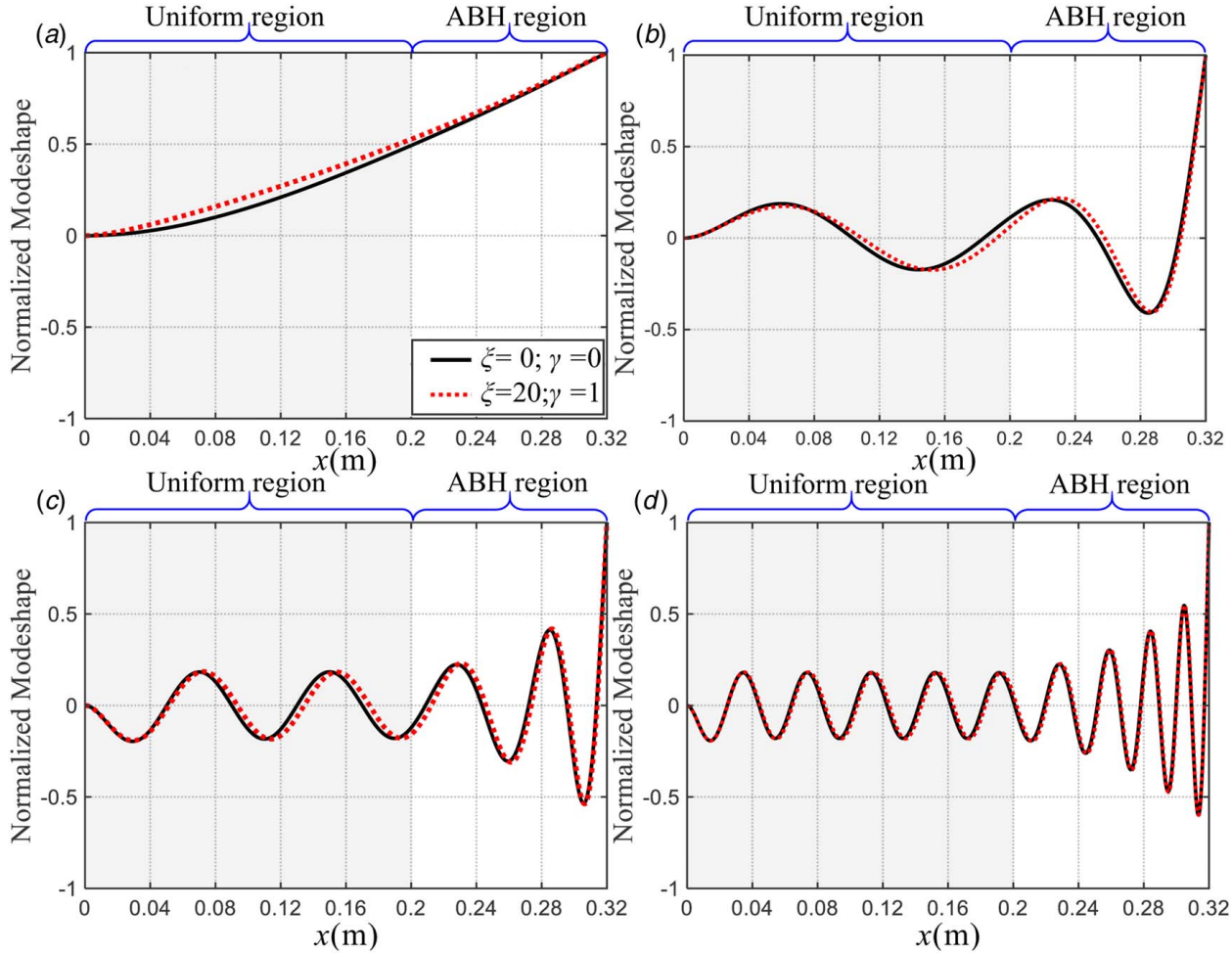

Fig. 5 Comparisons between the static and rotating conditions for (*a*) 1st mode, (*b*) 5th mode, (c) 10th mode, and (*d*) 20th mode shapes

obvious and the spinning-induced stiffness increase is not big enough to sensibly affect the system.

3.3 Spinning Effect on the Dynamics and Energy Transport in Acoustic Black Hole Beam. The dynamic response and vibrational energy transmission in spinning ABH beams under an external excitation are investigated. A point force with unit amplitude is applied at $x_f = 0.1$ m on the ABH beam. Different cases, without or with damping layers (denoted by DL in figures), are considered. When they are present, the damping layers cover the upper and bottom surface of the ABH beam from $x_{d1} = 0.28$ m to $x_{d2} = 0.32$ m with a constant thickness of $h_d = 0.0002$ m. Other geometric and material parameters used in the simulation are the same as those listed in Table 1.

Figure 6(*a*) presents the cross-point mobility at the observing point $x = 0.3$ m in the non-uniform region for four different cases.

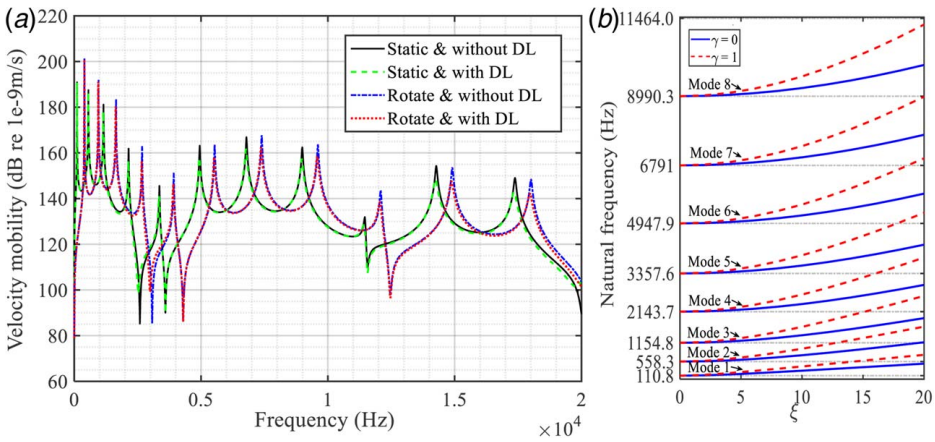

Fig. 6 (*a*) The cross-point mobility at $x = 0.3$ m on the ABH beam under four different status and (*b*) the variations of the first eight natural frequencies of the ABH beam under varying rotational velocity ξ and different hub radius γ

Comparing the static case (solid line) and rotating (dot-dash line) cases without damping layers and the other two cases with damping layers (dash line and dotted line), it can be seen that the dynamics of the beam is obviously affected by the spinning effect, as evidenced by an obvious shifting of the resonant peaks to higher frequencies, which can also be observed clearly from the Campbell diagram Fig. 6(*b*) of the variation of the first eight natural frequencies of the spinning ABH beams under varying rotational velocity ξ and different hub radius γ. It should be noted that, from Fig. 6(*b*), different from a rotating shaft or disk [24], which rotates with respect to the central axis of the structure, the ABH beam investigated in this work rotates with respect to the clamped end ($x = 0$) like a blade. As such, no splitting of the modes (forward and backward modes as observed in Ref. [24]) occurs as demonstrated in the literature [25] on rotating structures similar to ours. As expected, the deployment of the damping layer reduces the resonance peaks, which is rather significant considering the small amount of damping materials used. This partly reflects the damping enhancement phenomena in the system due to the ABH effects, which is not quite different from what one might expect when the beam is at rest.

The previous observation seems to allude that the ABH effect in a spinning ABH beam persists, although analysis of mode shapes also indicates a stretching of the wavelength in terms of modal deformation for some modes. Note the latter is less desirable since it might indicate an increase in the wave speed due to the spinning, which might adversely affect the expected ABH effects. In order to ascertain the effective occurrence of the ABH effects and quantify the influence of the rotation, the modal damping factors of the system are scrutinized. The modal loss factors are calculated by $\eta_n = \text{imag}(\omega_n^2)/\text{real}(\omega_n^2)$, with ω_n being the annular frequency (n is the mode order and $n = 1, 2, 3, \ldots$). More specifically, the overall modal loss factors of the system under different conditions are calculated and compared in Fig. 7(*a*).

Cases under static and rotating conditions with damping layers are considered. For the former, the rotating non-dimensional parameters $\xi = 10$ and hub radius ratio $\gamma = 1$, and the thickness of the damping layer at each side of the beam is $h_d = 0.0002$ m, covering the beam portion from x_{d1}–$x_{d2} = 0.28$–0.32 m. Note that with the damping layers, the inherent material loss factor of the beam is 0.5% and the corresponding damping loss factor is displayed, as marked by the solid line in Fig. 7(*a*). It can be observed that the modal loss factor of static ABH beam with a thin damping layer marked by circle symbols has an obvious increase, which is caused by the ABH effect in the improvement of system damping. As for the spinning ABH beam with damping layers, beam spinning motion can affect and decrease the system loss factor, much more significantly for the lower-order modes, while there is still an obvious increase of the loss factor in comparison with its static counterpart without damping layers upon higher order modes. It is worth noting that the large differences between different modal damping values in Fig. 7(*a*) are mainly caused by two aspects. One is due to the ABH effect, which is absent at low frequencies (before cut-on) but overwhelming at high frequencies. On the other hand, this is due to the rotation-induced decrease of the modal loss factors for the lower-order modes.

It is relevant to further understand how the spinning effect adversely affects the system modal loss factors. Physically, a modal loss factor is defined as the ratio of the dissipated energy over system potential energy for a given structural mode. To understand the variation of the modal loss factors induced by the rotation, the overall vibrational level of the ABH beams, namely mean quadratic velocity (MQV), which represents the mean quadratic velocity over the whole ABH beams is calculated and displayed in Fig. 7(*b*). The vibrational level of the beam under rotation at the first four resonant frequencies is larger than those of the beam at rest, with a much narrower bandwidth. The phenomenon is similar when the ABH beams are covered by damping layers on the upper and lower surfaces of the ABH taper. This evidences the decreasing modal loss factors in the beam, as suggested in Fig. 7(*a*). This leads to an impairment of the effective modal loss factors of the system, more significantly for lower-order modes.

Nevertheless, Fig. 7(*a*) clearly indicates that the damping effects of the damping layer are significantly enhanced by the ABH effect, which can explain the increasing modal loss factors at higher frequencies above the cut-on frequency [26]. Therefore, it can be concluded that, despite the adverse effects of the spinning, the ABH effect still occurs in a spinning ABH structure, although ABH-enhanced system damping might be affected and the actual cut-on frequency might also be increased, all due to the spinning-induced structural hardening.

To explore the influence of the geometrical parameters on the spinning ABH beams, different geometrical parameters of ABH beams are considered, with the corresponding parameters displayed in Fig. 8 for cases 1, 2, and 3.

In these numerical examples, rotating parameters are $\xi = 10$ and $\gamma = 1$, and the material parameters are the same as in Table 1. The thickness of the damping layers covered on the upper and lower surfaces of the beam are $h_d = 0.0002$ m installed from x_{d1}–$x_{d2} = 0.28$–0.32 m for case 1 and x_{d1}–$x_{d2} = 0.31$–0.35 m for case 2 and case 3.

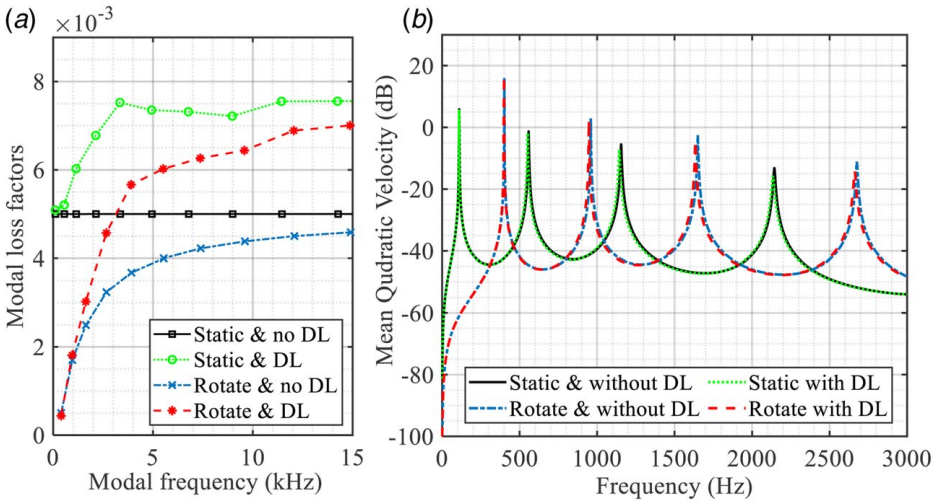

Fig. 7 (*a*) Modal loss factor of ABH beam under static and rotating statuses without/with damping layers and (*b*) the mean quadratic velocity over the whole ABH beam under static and rotating statuses without/with damping layers

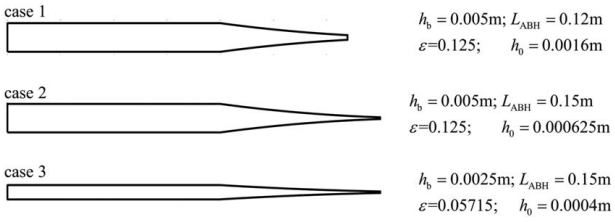

Fig. 8 Geometrical parameters of ABH beams in three cases

Comparisons in terms of the first eight natural frequencies of the rotating ABH beams among the three cases are displayed in Fig. 9. It can be seen that the rotation increases the natural frequencies in all three cases as expected. With reducing truncated thickness h_0 and the thickness of the uniform part h_b, the natural frequencies reduce as well, because of the reduced stiffness of the ABH beams when the thicknesses become thinner.

Figure 10 shows the variation of the modal loss factors of the spinning ABH beams for the same three cases under static/rotating conditions. The variation of the modal loss factors induced by the ABH effect and the spinning is influenced by the geometrical parameters, especially the truncated thickness h_0 and the thickness of the uniform part h_b. Comparing the results of cases 1, 2 and cases 2,3 in Fig. 10, it follows that a thinner h_0 and h_b will result in higher modal loss factors and lower modal frequencies (shadow area in Fig. 10), those the modal loss factors are larger than the inherent loss factors of the host beam. In another word, the modal loss factors will surpass the inherent loss factors of the host beam sooner with the ABH tips having thinner truncated thickness h_0.

Besides, the effects of the rotation on the ABH beams with different material parameters of the damping layers are examined, by taking the geometrical parameters of case 2 as an example. The host beam material parameters are the same as those listed in Table 1, and the material parameters of damping layers, including Young's modulus, mass density, and material loss factor, are selected and shown in Table 3.

Figure 11 compares the modal loss factors of the rotating ABH beams covered by damping layers with different material parameters. It can be seen that a stiffer damping material will result in higher modal loss factors in the spinning ABH beam since a stiffer material would store more energy and then the dissipated energy will also increase.

To further quantify the overall vibrational energy distribution of the rotating ABH beam over its different portions, the ratio of the mean quadratic velocity of the ABH portion to that of the uniform portion, defined as $\chi = 10\log[|v|^2_{ABH}/|v|^2_{uni}]$, is scrutinized for the ABH beam without damping layers, with results given in Fig. 12. Rotation moves χ curves to higher frequencies with very

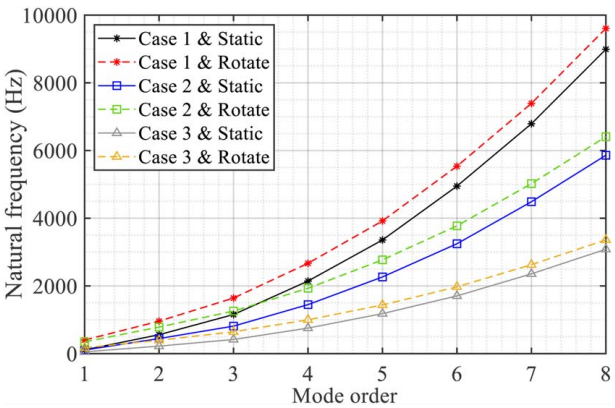

Fig. 9 The first eight natural frequencies of the rotating ABH beams for three cases

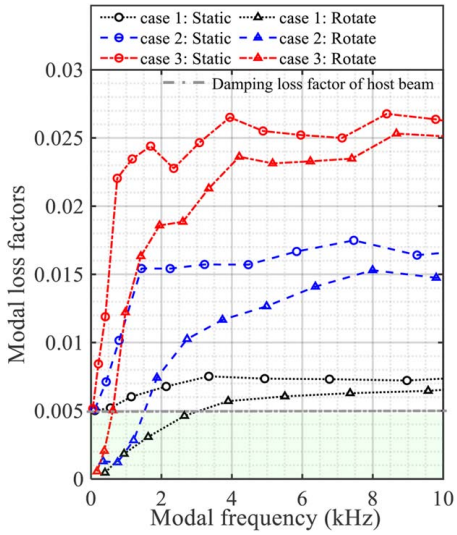

Fig. 10 The variations of the modal loss factors for the three cases under static/rotate conditions

Table 3 Material parameters of the damping layers

	Young's modulus	Mass density	Material loss factor
Material 1	$E_{d1} = 5$ GPa	$\rho_{d1} = 950$ kg/m^3	$\eta_{d1} = 0.3$
Material 2	$E_{d2} = 1$ GPa	$\rho_{d2} = 400$ kg/m^3	$\eta_{d2} = 0.9$

comparable overall levels. The fact the χ is larger than 0 dB in a large frequency range illustrates the fact that significant vibration does occur over the thin ABH portion, as compared with the uniform portion of the beam, in both static and rotating cases. This serves as another commonly accepted evidence of the occurrence of the ABH phenomena [4].

A particular feature, reconfirming the previously observed loss of the ABH effects in a structure of limited size at rest [27], can also be observed here even when the beam undergoes spinning. This region corresponds to cases where χ is significantly lower than 0 dB, as shadowed in Fig. 12. Obviously, as compared to its static counterpart, these regions corresponding to the loss of the ABH effect also move to higher frequencies.

To better understand the mechanism behind the observed ABH effect loss, the structural intensity distribution across the entire beam is examined. Three representative frequencies are singled out, as shown in Fig. 12. Two of them fall into the ABH effect loss region at $f_1 = 3602$ Hz (under static condition) and at $f_2 = 4292$ Hz (under rotating condition), while the third one is at $f_3 = 7574$ Hz, which is the cross point of two curves when the ABH effect is present. The structural intensity distributions at these three frequencies are compared in Fig. 13. According to the definition of structural intensity Eq. (27), positive and negative values of the structural intensity denote the power flow to the right and left directions of the beam passing through a given cross section, respectively. To eliminate the effect of total input power amplitude, the normalized structural intensity is utilized. The excitation position $x_f = 0.1$ m separates two different zones with positive and negative intensity values, in accordance with two opposite energy flow directions. It is clear that the vibrational energy flows into the beam structure from the excitation position and spreads over to both sides of the beam, with its amplitude gradually approaching zero at the two ends.

A closer examination of Fig. 13 allows for a better understanding of the loss phenomena of the ABH effect. Focusing first on 3602 Hz and 7574 Hz curves (beams at rest), representing two extreme cases

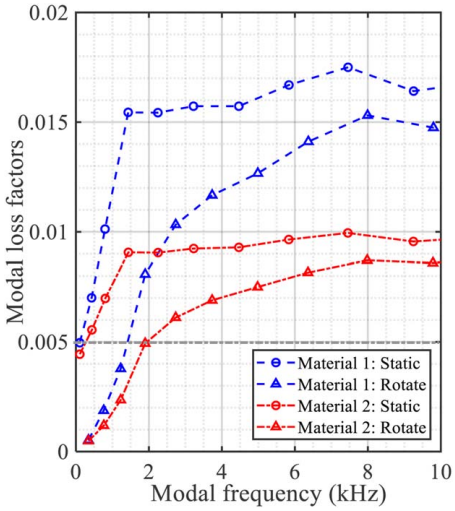

Fig. 11 Variation of the modal loss factors of the rotating ABH beams with different damping layer materials under static/rotating conditions

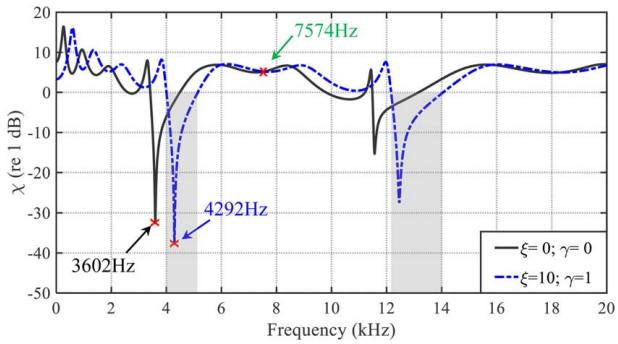

Fig. 12 Ratio of the mean quadratic velocity of ABH portion to uniform beam portion under static and rotating conditions

when the ABH effect is lost and preserved, respectively. It can be seen that at 7574 Hz, energy is spread out in both directions including the ABH part. This allows the expected ABH effects to fully play out as shown in the figure. At 3602 Hz, however, nearly the entire injected power goes to the uniform portion (left to the excitation point). Very little energy, if any, goes to the ABH portion, thus causing the observed ABH effect loss. The spinning of the beam does not fundamentally change the phenomena observed for beams at rest, except that the ABH loss effect takes place at a

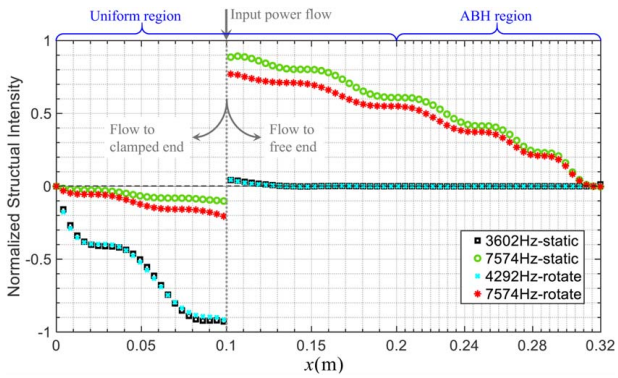

Fig. 13 Comparison of structural intensity distributions under three different frequencies and two states of the ABH beam

higher frequency (4292 Hz). Meanwhile, even when the ABH effect is present, the spinning seems to reduce the amount of energy flowing toward the ABH portion while increasing that toward the left hand-side portion. This offers a supplementary explanation of the aforementioned compromised ABH effects due to spinning since the energy flowing into the ABH portion is reduced.

To further demonstrate the effects of the spinning, the normalized structural intensity at three representative observation points of the spinning beam, x_1 (0.16 m), x_2 (0.21 m), and x_3 (0.26 m), is calculated in the frequency domain with rotating speed ratio ξ varying from 0 to 20. Same as before, a unit excitation force is applied at $x_f = 0.1$ m, by only considering the inherent structural damping, the calculated results are displayed in Fig. 14. It can be seen that, for each given position, energy flowing through it to the ABH tip direction is obviously frequency dependent. In particular, the dark color bands correspond to the regions discussed before when the ABH effects are lost. Once again, the very low level of the structural intensity within these bands reconfirms that the energy going toward the ABH tip direction is minimal. It is also obvious that these bands, together with the overall structural intensity distribution across the frequency range are increased when the spinning speed increases. Comparing the three diagrams for the three different points, it can be seen that, although the overall variation trends and distributions of the structural intensity are very similar, there is a clear reduction in the magnitude when moving further away from the excitation point to the ABH tip. This is a clear indication that the vibrational energy is gradually dissipated while flexural waves propagate along the beam toward the free end. Since the three points are equally spaced along the beam, it can be seen that the reduction in the structural intensity becomes more significant when approaching the ABH tip.

It is expected that the deployment of damping layers over the ABH portion would further enhance the above phenomena. To demonstrate this and to show the spatial distribution of the structural intensity over the entire structure, structural intensity analysis is performed for the same ABH beam without and with damping layers when the beam is at rest or rotating. Results are presented in Fig. 15. The DL cover from $x_{d1} = 0.28$ m to $x_{d2} = 0.32$ m with its thickness as $h_d = 0.0002$ m symmetrical to the neutral plane of the ABH beam.

For all cases, Fig. 15 shows that the force excitation injects energy into the structure, which is separated to flow into the left and right portions, represented by the region on the left (negative in colorbar) and the region on the right (positive in colorbar) of the excitation point, respectively. The darkest color strips on the left of the excitation correspond to the frequency ranges in which the ABH effects are lost, as discussed before. When the ABH

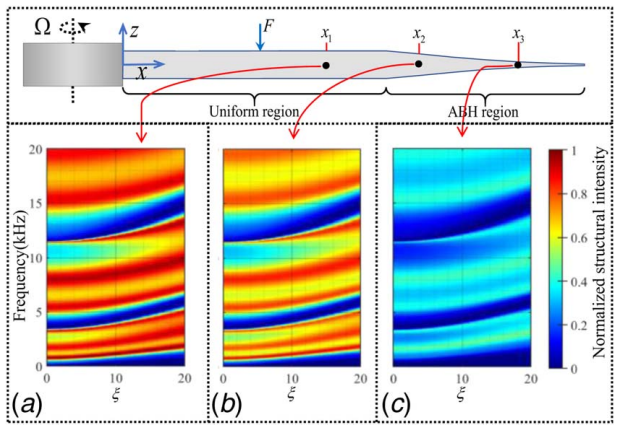

Fig. 14 Normalized structural intensity at three representative positions: (*a*) x_1, (*b*) x_2, and (*c*) x_3 in the frequency domain with rotating speed variation

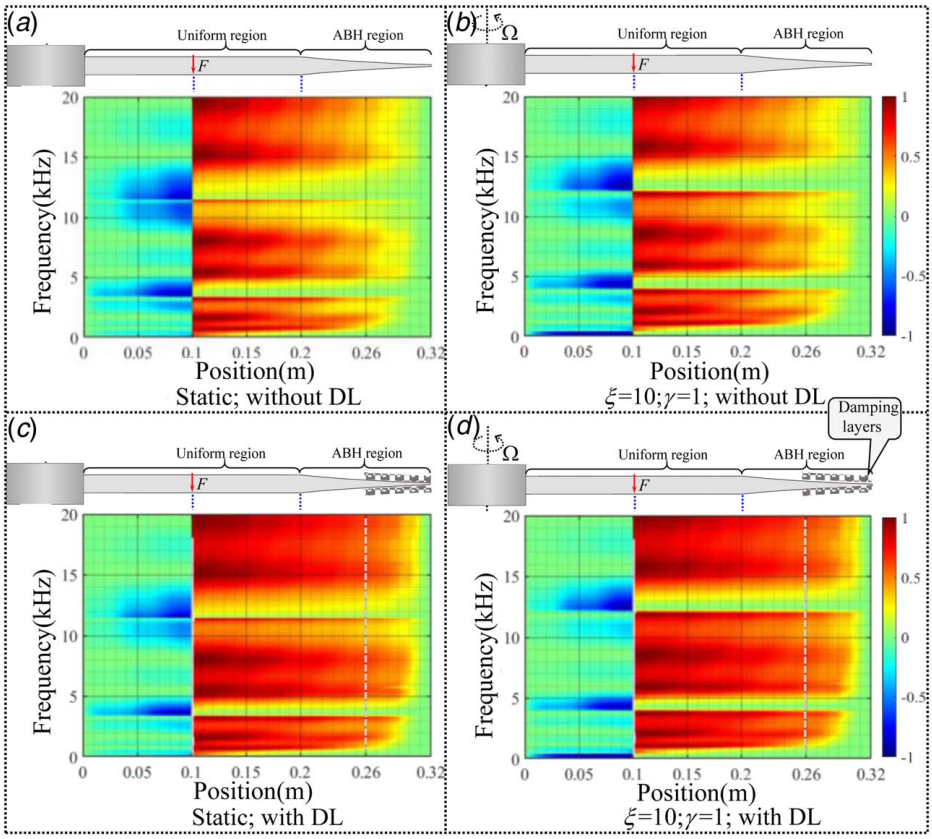

Fig. 15 Normalized structural intensity distribution in the frequency domain under the static and rotating conditions with or without damping layers

beam tip is covered with damping layers, the local damping over the coated region obviously increases (area on the right of the excitation point), thus attracting more energy into the region before being dissipated by the damping layers. Figures 15(*a*) and 15(*c*) show that, even for the beam at rest, energy transmission to the ABH tip direction increases, evidenced by an overall increase in both the intensity (darker color) and an enlarged area. This means that with the damping layer, energy flows more easily toward the ABH tip and effectively and most dominantly dissipated by the damping layers. By the same token, wave reflection from the tip, and the bouncing back to the left-hand side of the beam (as negative structural intensity) is also reduced. This explains the intensified and enlarged positive intensity area discussed before. Most importantly, the beneficial role that the damping layer plays here, in terms of enhanced energy dissipation and reduced wave reflection, is the essence of the ABH phenomena. Examining Figs. 15(*b*) and 15(*d*) suggests that the aforementioned phenomena still persist even when the beam undergoes spinning.

4 Conclusions

Possible occurrences of the ABH phenomenon and the underlying physical mechanism in a beam undergoing high-speed spinning are investigated in this paper. A semi-analytical model of an elastically restrained Euler–Bernoulli spinning ABH beam with fully coupled damping layers symmetrically placed over the ABH tip is first established. The model is validated against numerical results from finite element analyses. Numerical analyses are then presented to investigate some salient vibration and wave propagation features pertinent to the spinning ABH beam by examining its dynamics, modal properties, and energy flow.

The prevailing conclusion arising from the analyses is that ABH effects, albeit affected, can still be produced in a high-speed spinning ABH beam, with nevertheless behaviors different from a beam at rest due to the spinning effects. The spinning creates centrifugal forces inside the beam, which leads to a hardening of the overall structural stiffness. In addition to an expected shift in the natural frequencies of the structure, a stretching of the wavelength of the modal deformation as compared with its counterpart at rest is observed, which is more obvious for some lower-order modes toward the clamped part of a cantilever beam. Because of this and the fact that energy flow to the ABH portion of the beam is also adversely affected by the spinning, the overall damping enhancement effect of the viscoelastic coating, as reflected by the overall structural damping factors, is not as significant as when the beam is at rest. Despite this, the use of a small percentage of damping materials around the ABH tip region in the form of viscoelastic coating still shows great benefit in facilitating energy flow to the ABH portion, before being trapped and dissipated. All in all, this study confirms that salient ABH features relating to wave compression, energy trapping, and dissipation, though affected by the spinning effects, are still persistent in a high-speed spinning structure. This points at the possibility of incorporating ABH principles in the design of some rotating mechanical components such as turbine blades.

Acknowledgment

This work is supported by the National Natural Science Foundation of China (Grant Nos. U2241261, 11972125, and 12102101) and Research Grant Council of the Hong Kong SAR (PolyU 152023/20E).

Conflict of Interest

There are no conflicts of interest.

Data Availability Statement

The data sets generated and supporting the findings of this article are obtainable from the corresponding author upon reasonable request.

References

[1] Mironov, M. A., 1988, "Propagation of a Flexural Wave in a Plate Whose Thickness Decreases Smoothly to Zero in a Finite Interval," Sov. Phys. Acoust., **34**(3), pp. 318–319.

[2] Krylov, V. V., 2004, "New Type of Vibration Dampers Utilising the Effect of Acoustic 'Black Holes'," Acta Acust. United Acust., **90**(5), pp. 830–837.

[3] Krylov, V. V., and Winward, R. E. T. B., 2007, "Experimental Investigation of the Acoustic Black Hole Effect for Flexural Waves in Tapered Plates," J. Sound Vib., **300**(1–2), pp. 43–49.

[4] Tang, L. L., Cheng, L., Ji, H. L., and Qiu, J. H., 2016, "Characterization of Acoustic Black Hole Effect Using a One-Dimensional Fully-Coupled and Wavelet-Decomposed Semi Analytical Model," J. Sound Vib., **374**, pp. 172–184.

[5] Wang, Y., Du, J., and Cheng, L., 2019, "Power Flow and Structural Intensity Analyses of Acoustic Black Hole Beams," Mech. Syst. Signal Process, **131**, pp. 538–553.

[6] Conlon, S. C., Fahnline, J. B., and Semperlotti, F., 2015, "Numerical Analysis of the Vibroacoustic Properties of Plates With Embedded Grids of Acoustic Black Holes," J. Acoust. Soc. Am., **137**(1), pp. 447–457.

[7] Bowyer, E. P., and Krylov, V. V., 2015, "Experimental Study of Sound Radiation by Plates Containing Circular Indentations of Power-Law Profile," Appl. Acoust., **88**, pp. 30–37.

[8] Deng, J., Guasch, O., and Zheng, L., 2021, "Reconstructed Gaussian Basis to Characterize Flexural Wave Collimation in Plates With Periodic Arrays of Annular Acoustic Black Holes," Int. J. Mech. Sci., **194**, p. 106179.

[9] Tang, L. L., and Cheng, L., 2017, "Enhanced Acoustic Black Hole Effect in Beams With a Modified Thickness Profile and Extended Platform," J. Sound Vib., **391**, pp. 116–126.

[10] Climente, A., Torrent, D., and Sanchez-Dehesa, J., 2013, "Omnidirectional Broadband Insulating Device for Flexural Waves in Thin Plates," J. Appl. Phys., **114**(21), p. 214903.

[11] Zhu, H., and Semperlotti, F., 2015, "Phononic Thin Plates With Embedded Acoustic Black Holes," Phys. Rev. B, **91**(10), p. 104304.

[12] Zhu, H., and Semperlotti, F., 2015, "Improving the Performance of Structure Embedded Acoustic Lenses via Gradient-Index Local Inhomogeneities," Int. J. Smart Nano Mater., **6**(1), pp. 1–13.

[13] Zhao, L. X., Conlon, S. C., and Semperlotti, F., 2014, "Broadband Energy Harvesting Using Acoustic Black Hole Structural Tailoring," Smart Mater. Struct., **23**(6), p. 065021.

[14] Zhao, L. X., Conlon, S. C., and Semperlotti, F., 2015, "An Experimental Study of Vibration-Based Energy Harvesting in Dynamically Tailored Structures With Embedded Acoustic Black Holes," Smart Mater. Struct., **24**(6), p. 065039.

[15] Li, X., and Ding, Q., 2019, "Sound Radiation of a Beam With a Wedge-Shaped Edge Embedding Acoustic Black Hole Feature," J. Sound Vib., **439**, pp. 287–299.

[16] Ma, L., and Cheng, L., 2019, "Sound Radiation and Transonic Boundaries of a Plate With an Acoustic Black Hole," J. Acoust. Soc. Am., **145**(1), pp. 164–172.

[17] Pelat, A., Gautier, F., Conlon, S. C., and Semperlotti, F., 2020, "The Acoustic Black Hole: A Review of Theory and Applications," J. Sound Vib., **476**, p. 115316.

[18] Gautier, F., and Krylov, V. V., 2020, "Special Issue: Recent Advances in Acoustic Black Hole Research," J. Sound Vib., **476**, p. 115335.

[19] Zhao, C. H., and Prasad, M. G., 2019, "Acoustic Black Holes in Structural Design for Vibration and Noise Control," Acoustics, **1**(1), pp. 220–251.

[20] Bayod, J., 2011, "Application of Elastic Wedge for Vibration Damping of Turbine Blade," J. Syst. Des. Dyn., **5**(5), pp. 1167–1175.

[21] Bowyer, E. P., and Krylov, V. V., 2014, "Damping of Flexural Vibrations in Turbofan Blades Using the Acoustic Black Hole Effect," Appl. Acous., **76**, pp. 359–365.

[22] Banerjee, J. R., and Sobey, A. J., 2002, "Energy Expressions for Rotating Tapered Timoshenko Beams," J. Sound Vib., **254**(4), pp. 818–822.

[23] Du, J. T., Li, W. L., Liu, Z. G., Yang, T. J., and Jin, G. Y., 2011, "Free Vibration of Two Elastically Coupled Rectangular Plates With Uniform Elastic Boundary Restraints," J. Sound Vib., **330**(4), pp. 788–804.

[24] Lee, C. W., and Ham, J. S., 1999, "Mode Identification for Rotating Rigid Shaft With Flexible Disks by Mode Splits," J. Sound Vib., **225**(3), pp. 425–446.

[25] Yoo, H. H., and Shin, S. H., 1998, "Vibration Analysis of Rotating Cantilever Beams," J. Sound Vib., **212**(5), pp. 807–828.

[26] Lee, J. Y., and Jeon, W., 2021, "Wave-Based Analysis of the cut-on Frequency of Curved Acoustic Black Holes," J. Sound Vib., **492**, p. 115731.

[27] Tang, L. L., and Cheng, L., 2016, "Loss of Acoustic Black Hole Effect in a Structure of Finite Size," Appl. Phys. Lett., **109**(1), p. 014102.